

ARTICLE

DOI: 10.1038/s41467-017-00152-z

OPEN

Synthesis of ordered carbonaceous frameworks from organic crystals

Hiroto Nishihara^{1,2}, Tetsuya Hirota¹, Kenta Matsuura¹, Mao Ohwada¹, Norihisa Hoshino¹, Tomoyuki Akutagawa¹, Takeshi Higuchi¹, Hiroshi Jinnai¹, Yoshitaka Koseki¹, Hitoshi Kasai¹, Yoshiaki Matsuo³, Jun Maruyama⁴, Yuichiro Hayasaka⁵, Hisashi Konaka⁶, Yasuhiro Yamada⁷, Shingi Yamaguchi⁸, Kazuhide Kamiya^{2,9}, Takuya Kamimura¹⁰, Hirofumi Nobukuni¹⁰ & Fumito Tani¹⁰

Despite recent advances in the carbonization of organic crystalline solids like metal-organic frameworks or supramolecular frameworks, it has been challenging to convert crystalline organic solids into ordered carbonaceous frameworks. Herein, we report a route to attaining such ordered frameworks via the carbonization of an organic crystal of a Ni-containing cyclic porphyrin dimer (Ni₂-CPD_{py}). This dimer comprises two Ni-porphyrins linked by two butadiyne (diacetylene) moieties through phenyl groups. The Ni₂-CPD_{py} crystal is thermally converted into a crystalline covalent-organic framework at 581 K and is further converted into ordered carbonaceous frameworks equipped with electrical conductivity by subsequent carbonization at 873–1073 K. In addition, the porphyrin's Ni-N₄ unit is also well retained and embedded in the final framework. The resulting ordered carbonaceous frameworks exhibit an intermediate structure, between organic-based frameworks and carbon materials, with advantageous electrocatalysis. This principle enables the chemical molecular-level structural design of three-dimensional carbonaceous frameworks.

¹Institute of Multidisciplinary Research for Advanced Materials, Tohoku University, 2-1-1 Katahira, Aoba, Sendai 980-8577, Japan. ²PRESTO, the Japan Science and Technology Agency (JST), 4-1-8 Honcho, Kawaguchi 332-0012, Japan. ³Department of Materials Science and Chemistry, Graduate School of Engineering, University of Hyogo, 2167 Shosha Himeji, Hyogo 671-2280, Japan. ⁴Research Division of Environmental Technology, Osaka Research Institute of Industrial Science and Technology, 1-6-50, Morinomiya, Joto-ku, Osaka 536-8553, Japan. ⁵The Electron Microscopy Centre, Tohoku University, 2-1-1 Katahira, Aoba, Sendai 980-8577, Japan. ⁶Application & Software Development Department, X-ray Instrument Division, Rigaku Corporation, 3-9-12 Matsubara-cho, Akishima-shi, Tokyo 196-8666, Japan. ⁷Graduate School of Engineering, Chiba University, 1-33 Yayoi, Inage, Chiba 263-8522, Japan. ⁸Department of Applied Chemistry, The University of Tokyo, 7-3-1 Hongo, Bunkyo-ku, Tokyo 113-8656, Japan. ⁹Research Center for Solar Energy Chemistry, Osaka University, 1-3 Machikaneyama, Toyonaka, Osaka 560-8531, Japan. ¹⁰Institute for Materials Chemistry and Engineering, Kyushu University, 744 Motooka, Nishi-ku, Fukuoka 819-0395, Japan. Correspondence and requests for materials should be addressed to H.N. (email: hirotomo.nishihara.b1@tohoku.ac.jp) or to F.T. (email: tanif@ms.ifoc.kyushu-u.ac.jp)

Carbonaceous materials are generally prepared by carbonization of organic substances. During the carbonization process, organic precursors are thermally converted into aggregations of imperfect graphene fragments via intermediates of polycyclic aromatic compounds¹. Despite their complicated and random structures, carbonaceous materials possess many advantageous properties (electrical conductivity, chemical and thermal stability, light weight). Hence, they are used in a variety of applications including adsorbents, catalysts, supercapacitors, and polymer-electrolyte fuel cells (PEFCs)². When precursors like porphyrins and phthalocyanines with metal/nitrogen (M/N) are employed, their heteroatoms are dispersed in the resulting M/N/C composites³. Thus, they show great potential as non-Pt catalysts for oxygen-reduction reactions in PEFCs^{4–6}. The thermal conversion process for the production of these carbonaceous materials comprises complex, poorly controlled radical reactions¹. Hence, the molecular-level control of this process to realize next-generation, high-performance functional carbonaceous materials is challenging. To overcome this, carbonization of molecular-based crystals (metal-organic frameworks^{7–16}/molecular organic crystals^{17, 18}) with well-designed chemical and supramolecular structures has been employed. This controls the process indirectly via the chemical structures of the precursors while retaining the bulk particle morphology^{8, 10} and/or approximate porosity¹⁷, even after carbonization. However, molecular-based crystals convert into intrinsically amorphous carbonaceous frameworks and the precursor structure and molecular features are totally lost during carbonization. Structure-preserving carbonization has only been achieved in mesoscopic organic structures (>5 nm) formed by self-assembly of block-copolymers or surfactant templates^{19–21}. Moreover, the direct conversion of organic crystals into ordered carbonaceous frameworks (OCFs) has not been demonstrated.

Herein, we propose the design and supramolecular network structure of a precursor molecule. Our aim was to preserve the precursor structure, while converting a limited part into a carbonaceous framework, to synthesize hybrid materials. These are equipped with precursor structural and chemical features and carbon material properties. The cyclic porphyrin dimer ($\text{Ni}_2\text{-CPD}_{\text{Py}}$)²² met these criteria. $\text{Ni}_2\text{-CPD}_{\text{Py}}$ comprises

two Ni-porphyrins linked by two butadiyne (diacetylene) moieties through phenyl groups; each porphyrin includes two *meso*-pyridyl groups. The M-N₄ (M = metal) unit in the porphyrin ring is thermally stable (~973 K)^{23, 24}. Diacetylene is thermally polymerized to poly(diacetylene) to form a rigid crosslinked network, allowing the precursor morphology to be maintained during carbonization. $\text{Ni}_2\text{-CPD}_{\text{Py}}$ does not contain volatile fragments¹, thus, a high carbon yield essential to retain the overall framework morphology of the precursor crystal is predicted.

Results

Carbonization of $\text{Ni}_2\text{-CPD}_{\text{Py}}$. The molecular structure of $\text{Ni}_2\text{-CPD}_{\text{Py}}$ is shown in Fig. 1a. The thermal behaviour of $\text{Ni}_2\text{-CPD}_{\text{Py}}$ was investigated and compared to the corresponding free base porphyrin ($\text{H}_4\text{-CPD}_{\text{Py}}$)²⁵. Figure 1b displays weight changes of $\text{Ni}_2\text{-CPD}_{\text{Py}}$ and $\text{H}_4\text{-CPD}_{\text{Py}}$ measured by thermogravimetry (TG) in N₂ and their differential scanning calorimetry (DSC) curves. The molecules do not exhibit weight loss for temperatures ≤ 750 K, demonstrating excellent heat-stability and minimal volatility. Thus, $\text{Ni}_2\text{-CPD}_{\text{Py}}$ and $\text{H}_4\text{-CPD}_{\text{Py}}$ afforded high yields (91% and 77%, respectively, 1073 K). Their carbonization processes were further analysed by temperature-programmed desorption (TPD) with thermogravimetry/photoionization mass spectrometry (TG-PI-MS, Supplementary Fig. 1). Few species (C_6H_6 , C_5NH_5 , C_7H_8 , $\text{C}_4\text{NH}_5/\text{C}_5\text{H}_7$, C_5H_8 , and NH_3) were desorbed from $\text{Ni}_2\text{-CPD}_{\text{Py}}$, while a variety of species were found in $\text{H}_4\text{-CPD}_{\text{Py}}$, suggesting that limited decomposition occurs in $\text{Ni}_2\text{-CPD}_{\text{Py}}$. The carbonaceous residues afforded after TG measurement were analysed by transmission electron microscopy (TEM, Fig. 1c,d). The product derived from $\text{Ni}_2\text{-CPD}_{\text{Py}}$ displayed an ordered structure (periodicity = 14.7 Å). The corresponding electron diffraction pattern clearly differed from that of the graphite (002) plane (periodicity = 3.4 Å). Conversely, the $\text{H}_4\text{-CPD}_{\text{Py}}$ residue did not exhibit a highly ordered structure (Fig. 1d). Thus, the porphyrin cation significantly affected the carbonization process and the resulting structure. Ni stabilizes the porphyrin against the thermochemical decomposition, thereby achieving the better yield and retaining the ordered structure.

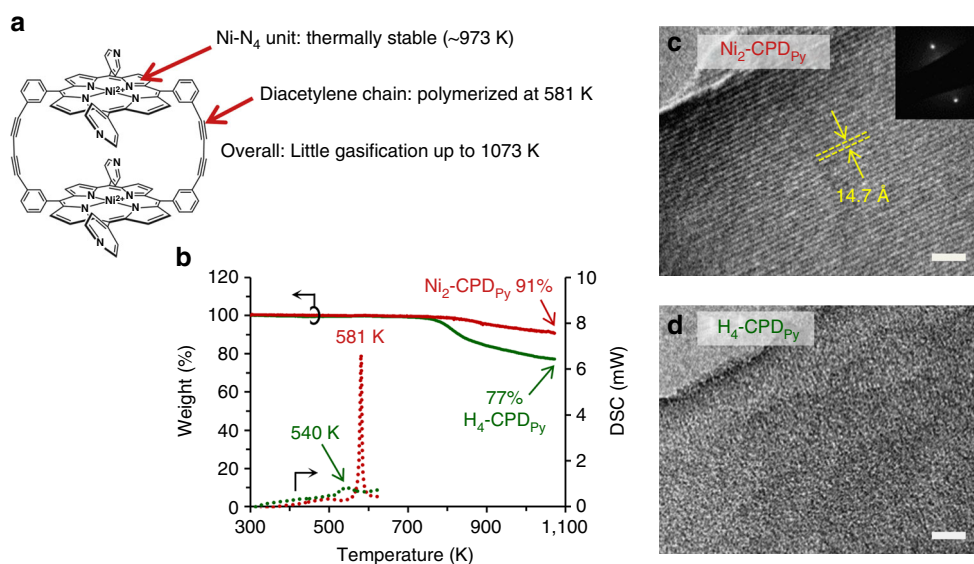


Fig. 1 Structure of $\text{Ni}_2\text{-CPD}_{\text{Py}}$ and its thermal properties up to a temperature of 1073 K. **a** Structure of $\text{Ni}_2\text{-CPD}_{\text{Py}}$ and its superior properties as a precursor of carbonization. **b** TG (solid lines) and DSC curves (dotted lines) of $\text{Ni}_2\text{-CPD}_{\text{Py}}$ (red) and $\text{H}_4\text{-CPD}_{\text{Py}}$ (green). Yields at 1073 K are described for TG curves, while peak temperatures are shown for DSC curves. **c**, **d** TEM images of the residues of **(c)** $\text{Ni}_2\text{-CPD}_{\text{Py}}$ and **(d)** $\text{H}_4\text{-CPD}_{\text{Py}}$ after TG measurements. Scale bars = 10 nm. Inset: a selected-area diffraction pattern for **c**

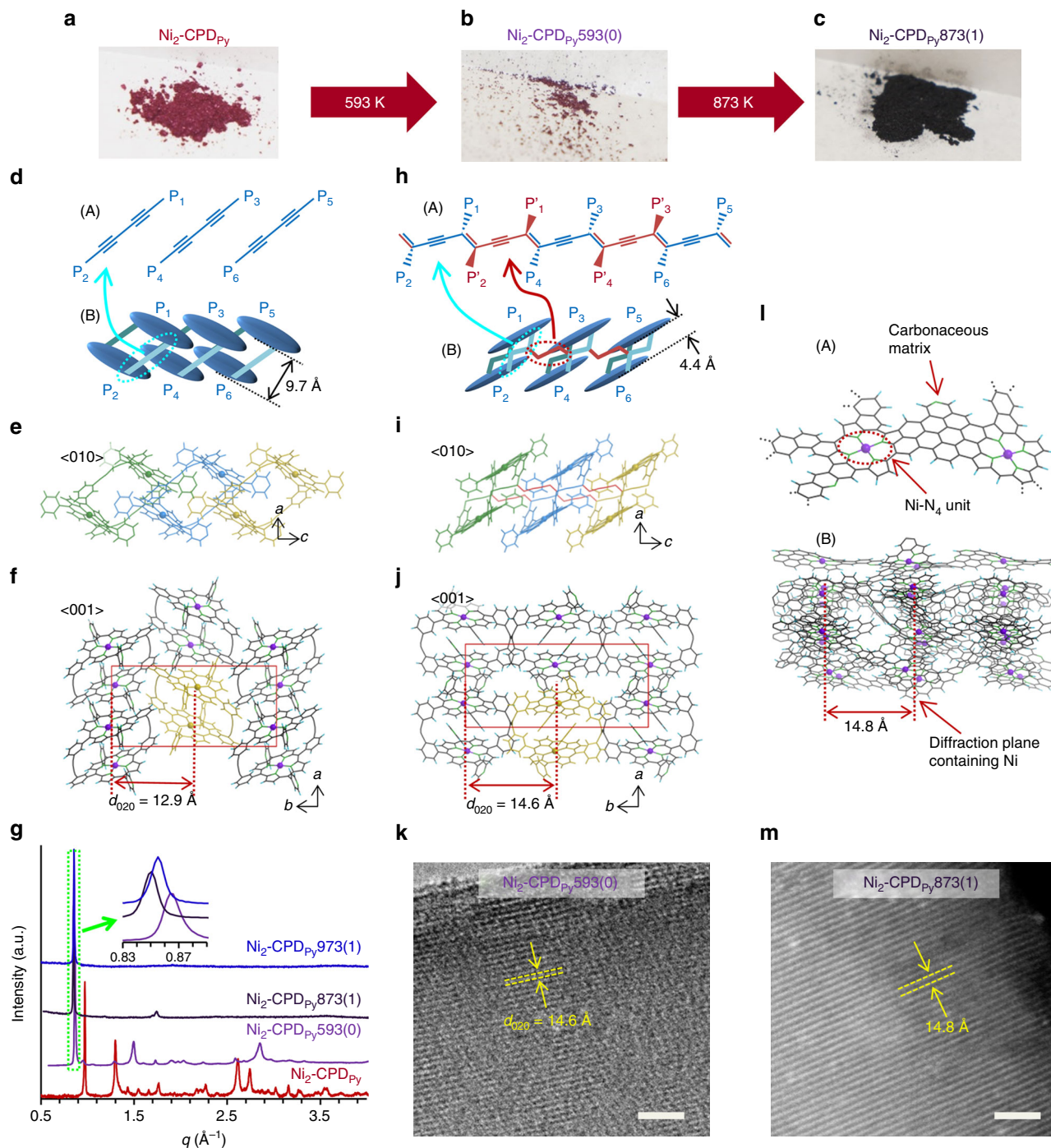


Fig. 2 Structure evolution of $\text{Ni}_2\text{-CPD}_{\text{Py}}$ upon heat-treatment. **a–c** Photographs of **(a)** $\text{Ni}_2\text{-CPD}_{\text{Py}}$, **(b)** $\text{Ni}_2\text{-CPD}_{\text{Py}593(0)}$, and **(c)** $\text{Ni}_2\text{-CPD}_{\text{Py}873(1)}$. **d** Schematic representation of diacetylene chains (A) and $\text{Ni}_2\text{-CPD}_{\text{Py}}$ molecules (B); P_n = porphyrin unit ($n = 1-6$). **e** Molecular structure of **d**-(B): bottom illustration, <010> direction; each molecule is displayed in a different colour. **f** Larger area view: <001> direction; yellow part corresponds to the yellow moiety in **e**. **g** PXRD patterns of $\text{Ni}_2\text{-CPD}_{\text{Py}}$ and heat-treated samples; inset: enlarged intense peaks of heat-treated samples. **h–j** $\text{Ni}_2\text{-CPD}_{\text{Py}593(0)}$ packing structure. **h** Schematic representation of part corresponding to **d**. In (A), porphyrins locate next to those shown in (B) are indicated with the symbol, P_n' . **i** Molecular structure of **h**-(B): <010> direction. Coloured moieties correspond to those in **e**. **j** Larger area view from the <001> direction; yellow part corresponds to the yellow moiety in **i**. Red box in **f** and **j** is unit cell. **k** TEM image of $\text{Ni}_2\text{-CPD}_{\text{Py}593(0)}$. **l** Expected molecular-level structure of $\text{Ni}_2\text{-CPD}_{\text{Py}873(1)}$; an enlarged part (A) and a larger region (B) corresponding to **j**. For **f**, **j**, and **l**: C, H, N, O, Ni = black, light blue, green, red, and purple, respectively. **m** HAADF-STEM image of $\text{Ni}_2\text{-CPD}_{\text{Py}873(1)}$. Scale bars in **k** and **m** are 10 nm

The $\text{Ni}_2\text{-CPD}_{\text{Py}}$ DSC curve (Fig. 1b) exhibits an intense exothermic peak at 581 K (integration = 142 J g^{-1} heat). This corresponds to 102 kJ mol^{-1} per diacetylene amount included in $\text{Ni}_2\text{-CPD}_{\text{Py}}$ and this value is ascribed mainly to the diacetylene heat of polymerization (well in agreement with

literature values: $80\text{--}151 \text{ kJ mol}^{-1}$)^{26, 27}. The $\text{H}_4\text{-CPD}_{\text{Py}}$ DSC curve exhibits a weaker peak at 540 K, affording 41 kJ mol^{-1} per diacetylene. This suggests that the cross-linking in $\text{H}_4\text{-CPD}_{\text{Py}}$ is not well developed, resulting in the collapse of the ordered structure (Fig. 1d).

Crystallographic structural changes upon carbonization. The structure evolution of Ni₂-CPD_{Py} upon heat treatment was analysed to understand the formation mechanism of the fine-ordered structure (Fig. 1c). Figure 2 summarizes the characterization results of Ni₂-CPD_{Py} and its heat-treated samples. Ni₂-CPD_{Py} almost retains its colour after polymerization [Ni₂-CPD_{Py},593(0)], indicating the preservation of the porphyrin unit (Fig. 2a,b). After carbonization, the sample turned black (Fig. 2c), confirming the conversion into a carbonaceous substance (graphene sheet formation). We previously reported the single-crystal structure of Ni₂-CPD_{Py} accommodating toluene as a guest²². Herein, we employed a guest-free crystal (Fig. 2d–f) as a precursor to exclude the effect of toluene and simplify the carbonization process. The crystallographic structure was solved by the direct space method^{28–30} and Rietveld refinement³¹ of the powder X-ray diffraction (PXRD) pattern (Fig. 2g and Supplementary Fig. 2). The Ni₂-CPD_{Py} molecule exhibits a slipped-conformation (Fig. 2d–f). This differed from the overlapped conformation of its single crystal form²², and the distance between the two porphyrins was determined as 9.7 Å. The Ni₂-CPD_{Py} molecules are aligned along the *c*-axis to form columnar arrangement (Fig. 2e), and the columns are integrated to form the structure shown in Fig. 2f (see the detail structure in Supplementary Fig. 3 and Supplementary Movie 1). The diacetylene moieties are located in both sides of the column along the *b* axis. This ordered arrangement enables solid-phase polymerization to form another crystalline phase (Fig. 2h–j) that was similarly solved (Supplementary Fig. 4). Due to polymerization, the distance between the two porphyrins shortens (4.4 Å) and the Ni₂-CPD_{Py} molecules along the *b* and *c* axes are cross-linked through a poly(diacetylene) backbone to form a two-dimensional sheet. These sheets are stacked to form a crystal structure (Fig. 2j and Supplementary Fig. 5, Supplementary Movie 2). The polymerization of diacetylene moieties into poly(diacetylene) backbone (Fig. 2d, h) is commonly observed in organic molecules^{26, 32}. Solid ¹³C NMR confirmed that the diacetylene moieties are almost completely cross-linked to form the poly(diacetylene) form (Supplementary Fig. 6). Thus, Ni₂-CPD_{Py},593(0) is insoluble in chloroform (good solvent for Ni₂-CPD_{Py}) and ¹H NMR and matrix-assisted laser desorption/ionization time-of-flight mass spectrometry (MALDI-TOF-MS) did not detect any remaining monomer/oligomers. The transformation from monomer crystal into a crystalline covalent-organic framework is ascribed to the close proximity of the diacetylene moieties in Ni₂-CPD_{Py} (Fig. 2d–f), allowing solid-phase polymerization to proceed. On the other hand, H₄-CPD_{Py} is not a highly crystalline solid, and its packing structure cannot be solved from the PXRD pattern in its guest-free form (Supplementary Fig. 7). H₄-CPD_{Py} has broad PXRD peaks, and it means that the solid contains irregular packing structures and distributed distances between diacetylene moieties, causing imperfect polymerization. Thus, the original packing structure collapses during pyrolysis (Supplementary Fig. 7).

Upon polymerization, the *d*-spacing (12.9 Å) of the original Ni₂-CPD_{Py} (020) plane increases to 14.6 Å (Fig. 2g) and its periodicity is clearly observed in the TEM image (Fig. 2k). The structure regularity of the (020) plane is well retained, even after heat treatment (873 K). This is confirmed by the sharp peak (inset of Fig. 2g; *d*-spacing = 14.8 Å) that exhibits a *d*-spacing that is slightly greater than that of its precursor polymer (14.6 Å). Generally, the carbonization of organic substances results in matrix shrinkage^{19, 20} because graphene and its stacked graphitic structure have atomically denser frameworks. Thus, the increase in *d*-spacing indicates the formation of low-density framework structures. The resulting Ni₂-CPD_{Py},873(1) was further analysed by high angle annular dark-field scanning transmission electron

Table 1 Elemental compositions of the samples

Sample	Elemental composition (wt%)				
	C	H	N	Ni	O
Ni ₂ -CPD _{Py} ^a	76.8	3.4	11.7	8.2	0
Ni ₂ -CPD _{Py} ,873(1)	75.7	2.0	10.5	9.1	2.7
Ni ₂ -CPD _{Py} ,973(1)	78.1	1.1	10.2	9.4	1.2

^aFor Ni₂-CPD_{Py}, the composition is calculated from its molecular formula.

microscopy (HAADF-STEM; Fig. 2m: white-coloured area = Ni atoms). Ni rarely forms nanoparticles or aggregates often generated in the carbonaceous residues of metal porphyrins^{33, 34} (an example is shown later in the carbonization of 5,10,15,20-tetraphenyl-21H,23H-porphine nickel(II) [Ni-TPP]). Ni and NiO formation was not detected, even by synchrotron PXRD analysis (Supplementary Fig. 8). The image in Fig. 2m well agrees with the TEM image (Supplementary Fig. 9). Notably, the ordered structure spreads to several hundred nanometers (Supplementary Fig. 9). The results of TEM, HAADF-STEM, and synchrotron PXRD reveal that Ni is not aggregated as Ni metal or NiO, and exists along the structure regularity derived from the (020) plane of its precursor. As shown later, Ni retains its original coordination structure (Ni–N₄) in the carbonaceous framework. Moreover, synchrotron PXRD (Supplementary Fig. 8) and fast Fourier transform TEM images (Supplementary Fig. 10) prove the presence of several diffraction planes other than the (020) plane and high-order planes in Ni₂-CPD_{Py},873(1). This indicates its well-ordered structure, similar to organic-based frameworks. Fig. 2l displays a possible Ni₂-CPD_{Py},873(1) framework built on experimental evidence (see Supplementary Methods about the details of model construction). Porphyrin moieties are linked by a carbonaceous matrix keeping the Ni–N₄ structure and their approximate original positions [Ni₂-CPD_{Py},593(0)]. Thus, Ni atoms form the diffraction plane observed by PXRD and TEM/STEM analysis. As represented by this model (3D view is provided in Supplementary Movie 3), Ni₂-CPD_{Py},873(1) exhibits an intermediate framework between an organic substance and carbon, making this material distinguishable from any other substances. Moreover, the sample carbonized at 973 K still retains structural regularity with very small shrinkage (Fig. 2g, *d*-spacing = 14.7 Å) confirming the excellent heat stability of the ordered structure.

Chemical structure transition upon carbonization. The change in elemental composition associated with carbonization is summarized in Table 1. The amount of hydrogen decreases with an increase in temperature suggesting growth of the graphene sheets. Generally, carbons formed at 873 K are still defective and include dangling bonds, which are oxidized upon exposure to air. Hence, Ni₂-CPD_{Py},873(1) contains a small amount of oxygen. At a higher carbonization temperature (973 K), the oxygen amount decreases, indicating a decrease in dangling bonds. This is attributed to further development of the graphene sheets. Notably, the N and Ni contents are well retained up to 973 K. Thus, a hybrid material containing a large fraction of heteroatoms can be produced.

The Ni₂-CPD_{Py} chemical structure transition was analysed by Raman spectroscopy (Fig. 3a). Some of the major peaks in the Raman spectrum of Ni₂-CPD_{Py} can be ascribed as follows: breathing, 1010 cm⁻¹; δ(C–H), 1230 and 1355 cm⁻¹; ν(C=C), 1500 and 1590 cm⁻¹; ν(C≡C), 2130 cm⁻¹; and ν(C–H), 3110 cm⁻¹, from the results of simulation using the Gaussian 09 software³⁵, (Supplementary Methods, Supplementary Figs. 11

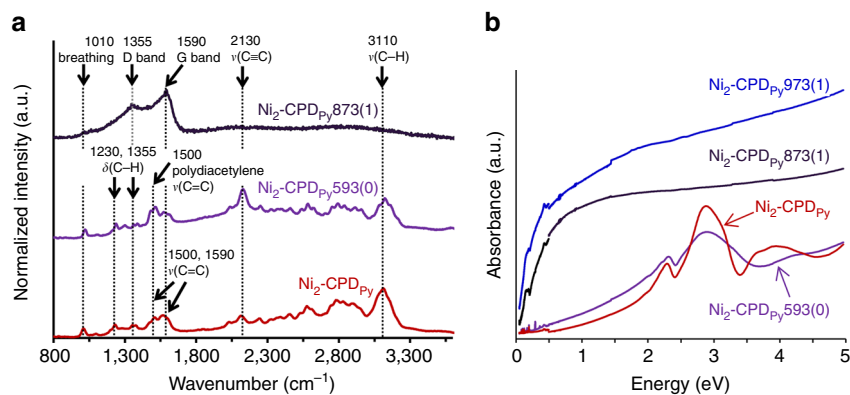


Fig. 3 Raman and UV-vis absorption spectra of $\text{Ni}_2\text{-CPD}_{\text{py}}$ and heat-treated samples. **a** Raman spectra: peak assignments are based on theoretical calculations (Supplementary Fig. 12) and references^{36, 39}. **b** Absorption spectra measured by FT-IR (<0.4959 eV) and UV-vis-NIR spectrometry (>0.4959 eV)

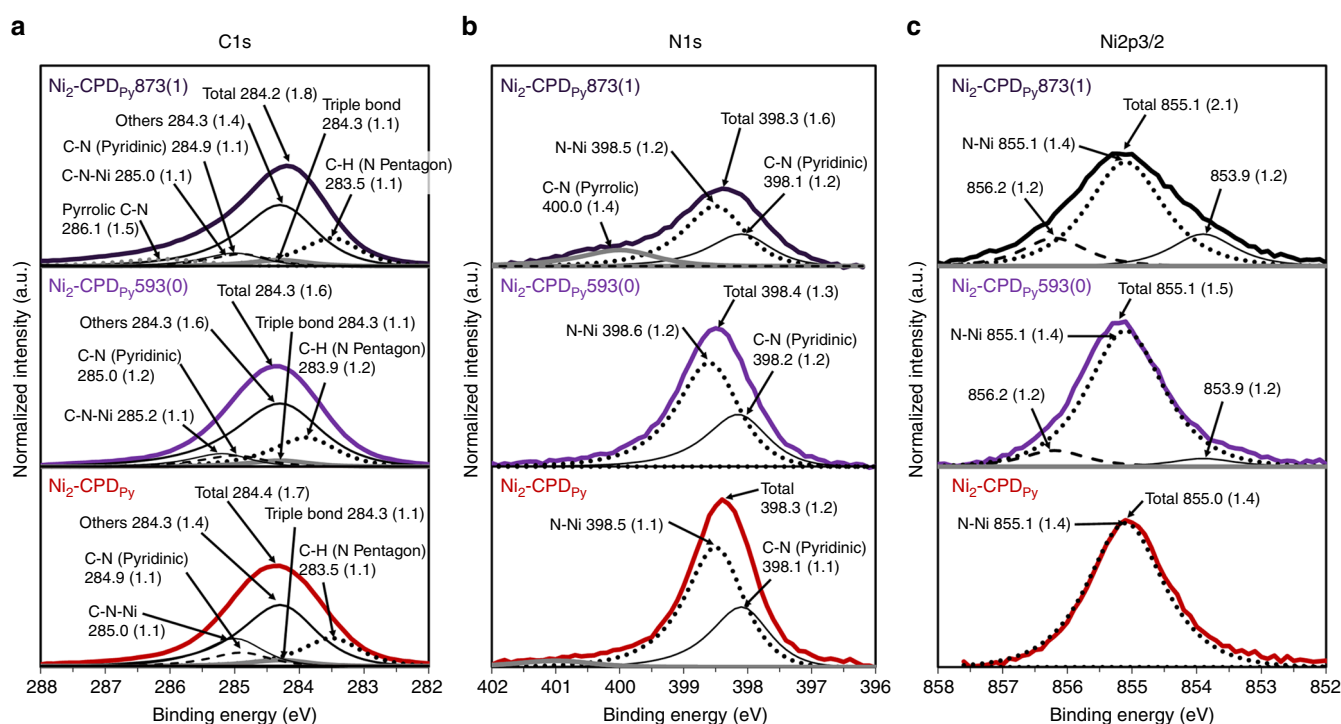


Fig. 4 X-ray photoelectron spectroscopy results of $\text{Ni}_2\text{-CPD}_{\text{py}}$ and heat-treated samples. **a** C1s, **b** N1s, **c** $\text{Ni}2p_{3/2}$. Numbers before parenthesis indicate binding energy in eV. Numbers inside the parenthesis indicate FWHM of spectra. In **a** and **b**, experimentally obtained peaks are deconvoluted into several peaks determined by theoretical calculations (Supplementary Fig. 16). In **c**, FWHM of the N-Ni peak is determined as 1.4 eV from the result of $\text{Ni}_2\text{-CPD}_{\text{py}}$, and the broadened parts in the heat-treated samples were deconvoluted into three peaks including two additional peaks that have lower (853.9 eV) and higher (856.2 eV) binding energies than that of N-Ni

and 12). Most peaks are retained in $\text{Ni}_2\text{-CPD}_{\text{py}593(0)}$; this is in agreement with the structure change shown in Fig. 2. A peak at 1500 cm^{-1} becomes intense in the polymer, and this reflects the formation of a poly(diacetylene) backbone (Supplementary Fig. 12). In $\text{Ni}_2\text{-CPD}_{\text{py}873(1)}$, most peaks disappear, and only broad D- and G-bands³⁶ originating from intervalley scattering^{37–39} appear, indicating that the well-defined chemical structure of the precursor polymer framework is lost and the resulting OCF consists of defective graphene sheets (Fig. 2l), like zeolite-templated carbons (ZTCs) and ordered mesoporous carbons². $\text{Ni}_2\text{-CPD}_{\text{py}}$ absorption spectrum (Fig. 3b) displays Q and Soret bands of the Ni^{2+} porphyrin unit (2.31 and 2.89 eV, respectively). Almost no energy shift is observed in $\text{Ni}_2\text{-CPD}_{\text{py}593(0)}$, strongly suggesting that the electric structures

of these units are retained in $\text{Ni}_2\text{-CPD}_{\text{py}593(0)}$. This agrees with the structure in Fig. 2h–j. Conversely, $\text{Ni}_2\text{-CPD}_{\text{py}873(1)}$ and $\text{Ni}_2\text{-CPD}_{\text{py}973(1)}$ display a broad absorption band from the mid-IR to UV region assigned to the interband transitions of the graphene sheets. Since the absorption of this transition is too strong, the absorption bands of the Ni^{2+} porphyrin unit are veiled and their presence cannot be confirmed in Fig. 3b. As shown later, the chemical states of Ni in the carbonized samples were analyzed also by X-ray absorption fine structure (XAFS) measurements of the Ni–K edge.

The formation of graphene sheets renders the OCFs electrically conductive. At room temperature, $\text{Ni}_2\text{-CPD}_{\text{py}}$ and $\text{Ni}_2\text{-CPD}_{\text{py}593(0)}$ were highly insulating (resistivity $\rho > 1\text{ T}\Omega\text{ cm}$). Meanwhile, in $\text{Ni}_2\text{-CPD}_{\text{py}873(1)}$ and $\text{Ni}_2\text{-CPD}_{\text{py}973(1)}$, a significant decrease

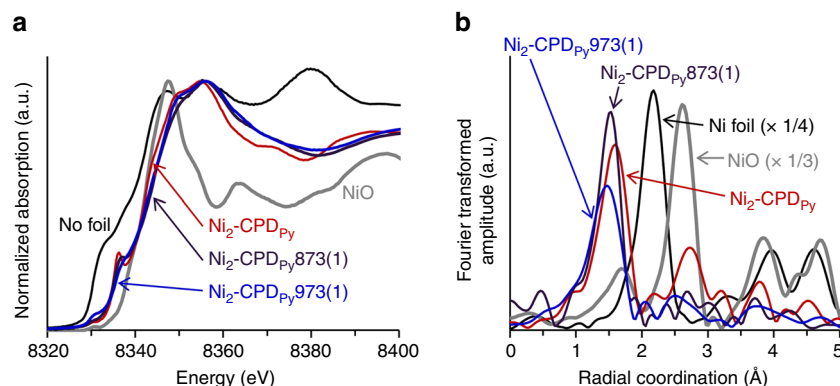


Fig. 5 X-ray absorption fine structure results of $\text{Ni}_2\text{-CPD}_{\text{py}}$ and its heat-treated samples. **a** XANES spectra. **b** Pseudo-radial structural functions calculated from EXAFS patterns. The data of Ni foil and NiO are also shown for comparison

in ρ (33.8 and 18.6 Ω cm, respectively at room temperature) was observed. Thus, unlike conventional organic-based frameworks, OCFs are equipped with electric conductivity. As the temperature decreased, both samples exhibited an increase in resistivity, indicating that both are semiconductors (Supplementary Fig. 13). The activation energies were estimated as 0.050–0.091 eV for $\text{Ni}_2\text{-CPD}_{\text{py},873(1)}$ and 0.015–0.022 eV for $\text{Ni}_2\text{-CPD}_{\text{py},973(1)}$. The microstructures of OCFs were further studied by X-band electron paramagnetic resonance (EPR) analysis (Supplementary Fig. 14). $\text{Ni}_2\text{-CPD}_{\text{py},873(1)}$ at 5.0 K displayed an absorption line ($g \sim 2$) with a sharp line-width (2.8 mT). These results indicate the formation of organic radicals derived from dangling bonds generated during the carbonization process. Conversely, $\text{Ni}_2\text{-CPD}_{\text{py},973(1)}$ exhibited broad absorptions and no signals attributed to radicals were observed. The broad peak is assigned to coupling with anisotropic spins in the six-coordinated paramagnetic Ni^{2+} ions generated during heat treatment. The structural change of $\text{Ni}_2\text{-CPD}_{\text{py}}$ was further analysed by X-ray photoelectron spectroscopy (XPS, Fig. 4). No significant changes were observed in the C1s, N1s, and $\text{Ni}2p_{3/2}$ XPS spectra during the transition from $\text{Ni}_2\text{-CPD}_{\text{py}}$ to $\text{Ni}_2\text{-CPD}_{\text{py},593(0)}$. This is explained by the change in structure shown in Fig. 2. The C1s spectra of $\text{Ni}_2\text{-CPD}_{\text{py}}$ and $\text{Ni}_2\text{-CPD}_{\text{py},593(0)}$ are well in agreement with results from theoretical calculations (Supplementary Figs. 15 and 16)^{35, 40–44} as well as the positions and full width at half maximum (FWHM) of the deconvolution peaks. Moreover, the C1s, N1s, and $\text{Ni}2p_{3/2}$ spectra of $\text{Ni}_2\text{-CPD}_{\text{py},873(1)}$ indicate that the chemical environment of these atoms differ only slightly from those in $\text{Ni}_2\text{-CPD}_{\text{py},593(0)}$, despite the disappearance of the well-defined phenyl groups, $\text{C}\equiv\text{C}$, and C-H bonds (Fig. 3a). In $\text{Ni}_2\text{-CPD}_{\text{py},873(1)}$, the N1s spectrum slightly broadens (change in FWHM) because of the appearance of a small C-N (pyrrolic) component at 400.0 eV. These moieties may be formed by thermal conversion of the pyridyl groups into the carbonaceous framework containing the pyrrolic structure, or by cleavage of porphyrin rings followed by hydrogen addition to the free pyrrolic N. The $\text{Ni}2p_{3/2}$ spectrum of $\text{Ni}_2\text{-CPD}_{\text{py}}$ broadens after heat treatment (two peak components at 856.2 and 853.9 eV). These components are ascribed to the oxidized Ni species, carbides, or metallic Ni^{45} .

Chemical environment of Ni in the carbon matrix. The XAFS of the Ni-K edge was also analysed by synchrotron X-ray absorption spectroscopy [X-ray absorption near edge structure (XANES) spectra in Fig. 5a]. The Ni-K edge energy (~ 8333 eV) of $\text{Ni}_2\text{-CPD}_{\text{py}}$ lies between those of Ni foil (8329 eV) and NiO (8336 eV). This reflects the intermediate oxidation state of Ni in $\text{Ni}_2\text{-CPD}_{\text{py}}$. The $\text{Ni}_2\text{-CPD}_{\text{py}}$ XANES spectrum exhibits a characteristic peak at

8336 eV, corresponding to the 1s to $4p_z$ transition⁴⁶. This is typical of a planar porphyrin⁴⁷ and phthalocyanine⁴⁶ where the Ni coordinates with four nitrogen atoms in the Ni- N_4 unit. Notably, the $\text{Ni}_2\text{-CPD}_{\text{py},873(1)}$ XANES spectrum is almost unchanged from that of $\text{Ni}_2\text{-CPD}_{\text{py}}$, indicating the retention of the Ni- N_4 unit even after carbonization. In $\text{Ni}_2\text{-CPD}_{\text{py},973(1)}$, a shoulder appears at 8329 eV, suggesting the formation of a small amount of metallic Ni due to the partial decomposition of the porphyrin moieties. However, the overall spectrum is still well retained.

The pseudo-radial structure functions were next calculated using the Ni-K edge extended X-ray absorption fine structure (EXAFS) spectra for $\text{Ni}_2\text{-CPD}_{\text{py}}$ and its carbonized derivatives, Ni foil, and NiO (Fig. 5b). $\text{Ni}_2\text{-CPD}_{\text{py}}$ exhibits an intense peak at 1.56 Å, corresponding to the four N atoms coordinated to the Ni atom. The carbonized samples display very similar patterns to that of $\text{Ni}_2\text{-CPD}_{\text{py}}$, confirming the retention of the Ni- N_4 unit after carbonization. The precise distance between Ni and N and its coordination number were calculated with FEFF8.2 (Supplementary Table 1). $\text{Ni}_2\text{-CPD}_{\text{py},873(1)}$ and $\text{Ni}_2\text{-CPD}_{\text{py},973(1)}$ retained the coordination numbers 3.8 and 3.4, respectively. This is close to the initial number (4).

The chemical environment of the Ni^{2+} ions was studied also by magnetic susceptibility analysis (Supplementary Fig. 17). Since Ni^{2+} ions in the square planar coordination geometry are diamagnetic, $\text{Ni}_2\text{-CPD}_{\text{py}}$ and $\text{Ni}_2\text{-CPD}_{\text{py},593(0)}$ seldom respond to an external magnetic field. Their minute responses are ascribed to minor impurities. $\text{Ni}_2\text{-CPD}_{\text{py},873(1)}$ retains a weak magnetization, indicating that the square planar coordination is well retained in the sample; this is in agreement with XAFS data. These samples almost obey the Curie-Weiss law in the range of 5.0–300 K, with small Curie constants ($C = 6.3 \times 10^{-6}$, 15×10^{-6} and $87 \times 10^{-6} \text{ cm}^3 \text{ g}^{-1} \text{ K}$, respectively). Conversely, $\text{Ni}_2\text{-CPD}_{\text{py},973(1)}$ data deviate from this law. This is attributed to the temperature-independent paramagnetic term, χ_p , corresponding to Pauli's paramagnetism of the graphene sheets and Ni metal cluster and agrees with results from XANES (Fig. 5a; curve fitting: $\chi_p = 13.7 \times 10^{-6} \text{ cm}^3 \text{ g}^{-1}$ and $C = 202 \times 10^{-6} \text{ cm}^3 \text{ g}^{-1} \text{ K}$). The increase in C is attributed to the generation of six-coordinated paramagnetic Ni^{2+} ions formed by heat treatment. If all the Ni^{2+} ions are converted into six-coordinated species, then $C = 1391 \times 10^{-6} \text{ cm}^3 \text{ g}^{-1} \text{ K}$ ($S = 1$, $g = 2.0$). Since the value of $\text{Ni}_2\text{-CPD}_{\text{py},973(1)}$ is 14.5% of this assumption, 85.5% of Ni^{2+} ions are expected to retain the square-planar coordination geometry, even after heat treatment at 973 K.

Electrochemical catalysis. Compared to carbon materials, organic-based frameworks have a great advantage of chemical

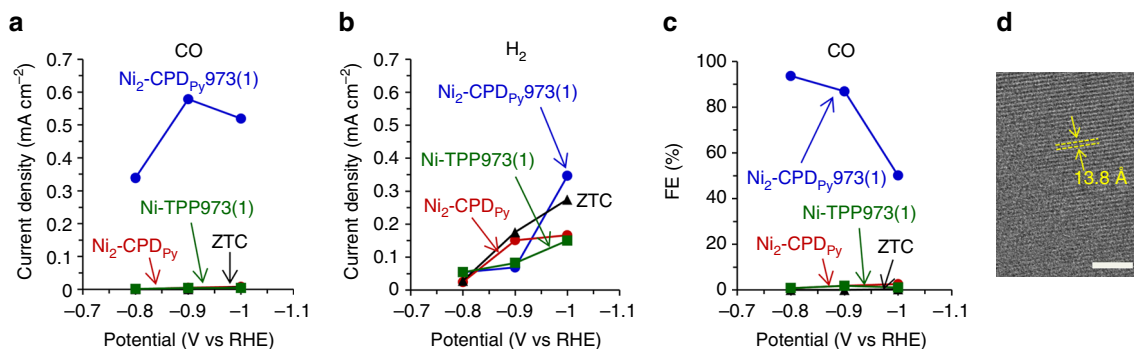


Fig. 6 Examination of selective CO₂ electro-reduction into CO. **a, b** Partial current densities used for **(a)** CO and **(b)** H₂ generation on the samples in CO₂-saturated 0.1M KHCO₃. **c** FE for CO generation. **d** TEM image of a reference ordered microporous carbon, ZTC

designability. In the latter materials, specific molecular blocks can be integrated three-dimensionally with structure order, by which a variety of unique functions can be achieved. However, they are intrinsically not electrically conductive unlike carbon, and are necessarily deposited as thin films on good conductors for electrochemical applications^{48–50}. The proposed OCFs are expected to provide new electrocatalyst designs in which active sites are embedded in electrically conductive frameworks with structure regularity. To prove this concept, we have examined the electrocatalytic activity of the porphyrin center (Ni–N₄ unit) retained in Ni₂-CPD_{Py}973(1). Unlike the cases of Fe and Co, Ni-based complexes are generally poor in electrocatalysis for oxygen-reduction reaction. However, specific Ni cyclam complexes^{51–54} or Ni-N-modified graphene⁵⁵, which have Ni–N₄ sites, have been reported to show unique electrocatalysis for the CO₂ reduction into CO without significant H₂ evolution and with a high Faradaic efficiency (FE) of ca. 90%. Additionally, this selective CO₂ reduction has rarely been reported in carbonaceous Ni/N/C materials made from Ni-based complexes. Figure 6 summarizes the comparison of selective CO₂ reduction activities of Ni₂-CPD_{Py}973(1) and three reference materials, characterized by the method reported elsewhere⁵⁵. Ni₂-CPD_{Py}973(1) shows apparent CO₂ reduction catalysis into CO (Fig. 6a) even without any conductive additives, while the activity for H₂ evolution is quite low below –0.9 V vs. RHE (reversible hydrogen electrode) (Fig. 6b). Thus, Ni₂-CPD_{Py}973(1) achieves high FE of 94 and 87% at –0.8 and –0.9 V, respectively (Fig. 6c). To further investigate the uniqueness of the OCF catalysis, the same measurement was applied to three reference materials: ZTC, Ni₂-CPD_{Py}, and Ni-TPP carbonized at 973 K for 1 h [Ni-TPP973(1)]. ZTC is an existing ordered microporous carbon prepared by using zeolite as a hard template², and has the structure periodicity of 13.8 Å (Fig. 6d), which is close to that of Ni₂-CPD_{Py}973(1). ZTC has an electrically conductive framework which comprises mainly of sp² carbons⁵⁶, but it does not possess catalysis sites including metal species. ZTC shows no catalysis in Fig. 6a, and this result clearly indicates that the ordered carbonaceous framework itself can never reduce CO₂. Ni₂-CPD_{Py} also shows no catalysis in Fig. 6a despite the presence of the Ni–N₄ unit, because the organic crystal of Ni₂-CPD_{Py} is not electrically conductive. Next, we discuss the active site. In the cases of Fe/N/C and Co/N/C electrocatalysts for oxygen reduction reaction, catalysis sites often exist as disordered forms consisting of metal species, N, and C. Hence, it is necessary to examine the catalytic activity of disordered Ni/N/C structure towards the selective CO₂ reduction into CO. For this purpose, Ni-TPP973(1) was prepared as a representative Ni/N/C material by the same carbonization procedure as that for Ni₂-CPD_{Py}973(1), from a common Ni-based porphyrin Ni-TPP. During the heat treatment, Ni-TPP is decomposed involving cleavage of Ni–N bonds, and it

turns into the mixture of a disordered Ni/N/C framework and Ni metal aggregation (Supplementary Fig. 18). The resulting Ni-TPP973(1) shows no catalysis in Fig. 6a, indicating that the disordered Ni/N/C structure is not active, and the Ni–N₄ unit is the active site in Ni₂-CPD_{Py}973(1). Figure 6 thus proves that the selective CO₂ reduction catalysis of Ni₂-CPD_{Py}973(1) can be achieved by the intermediate structure of organic-based frameworks and carbon materials, in which molecular catalysis sites (Ni–N₄) are embedded in the conductive framework. As mentioned above, conventional M/N/C catalysts have disordered structures and this has hampered the basic understanding between the structure and catalysis. With its certainly determined catalysis sites, Ni₂-CPD_{Py}973(1) can be a good platform to investigate the fundamentals of carbonaceous electrocatalysts.

The advantage of OCFs compared to conventional carbon materials is chemistry-based better controllability. Though the present OCFs are poorly porous (Supplementary Table 2), it is possibly improved by introducing volatile groups at designed sites of the starting molecules. Replacing Ni with other metals such as Fe, Co, Cu, Pt, and Pd can also widen the versatility of OCFs. Moreover, the exterior shape of the crystal can be also controlled based on the existing methods, for example a reprecipitation method^{57–60} (Supplementary Fig. 19) to achieve additional function⁵⁹. By their chemical designability, OCFs are expected to be further developed hereafter.

Discussion

In summary, the direct conversion of organic crystal into OCFs was demonstrated. The successive thermal conversion process actually comprises two steps. A molecular crystal of Ni₂-CPD_{Py} is first thermally converted into a crystalline covalent-organic framework, and is further converted into OCFs that inherit the periodic structure and the Ni–N₄ unit in the precursor organic crystal. The successful conversion is due to the following properties of Ni₂-CPD_{Py}. First, absence of volatile moieties like paraffin structures, oxygen, halogens, and sulphur. Second, presence of well-arrayed diacetylene moieties that can be thermally crosslinked to form a heat-stable polymer. Third, the presence of thermally stable (~973 K) organic moiety (metal porphyrin unit). On the basis of this strategy, a variety of OCFs could be synthesized, probably also from organic molecules other than Ni₂-CPD_{Py}. This new pathway allows the preparation of OCFs with molecularly controlled chemical structures that can be considered fusion materials of organic-based frameworks and carbon materials.

Methods

Materials. Ni₂-CPD_{Py} and H₄-CPD_{Py} were synthesized according to literature^{22, 25}. Heat treatment of Ni₂-CPD_{Py} and H₄-CPD_{Py} was performed at a heating rate of 5 K min^{–1} ramped at a designed temperature (593, 873, or 973 K, N₂ flow) by using a

tubular furnace. In the case of 593 K, heating was stopped immediately when the temperature reached 593 K. The samples thus obtained are Ni₂-CPD_{p_y}593(0) and H₄-CPD_{p_y}593(0). The sample name is expressed as follows: M-CPD_{p_y}X(Y) for M=Ni₂ or H₄, X is the treated temperature (K), and Y is the period of the treatment (h). In the case of 873 and 973 K, the temperature was maintained at the target temperatures for 1 h. As a reference, 5, 10, 15, 20-tetraphenyl-21H,23H-porphine nickel(II) (≥95%, Sigma-Aldrich) was carbonized at 973 K for 1 h by the same manner as that for Ni₂-CPD_{p_y}973(1). The sample thus obtained is Ni-TPP973(1). Zeolite-templated carbon was synthesized by the method reported elsewhere⁶¹.

Characterization. Porphyrin TG curves were measured by a Shimadzu TGA-51 thermogravimetric analyser (N₂ flow, ≤1073 K, H₄-CPD_{p_y}/Ni₂-CPD_{p_y}). TPD patterns were measured using a Rigaku ThermoMass Photo spectrometer (10 K min⁻¹, ≤1073 K, He flow). The afforded residue was observed by TEM (JEM-2010/JEM-2200FS, JEOL). DSC curves were recorded on a Mettler DSC1 STARE (≤623 K, 10 K min⁻¹, N₂ flow). To confirm the presence of the monomer/oligomers in Ni₂-CPD_{p_y}593(0), the sample was dispersed in chloroform and analysed by ¹H NMR (Bruker Avance III 400) and MALDI-TOF-MS (Bruker Autoflex Speed). ¹³C CP-MAS NMR spectra were measured on a JEOL JNM-ECA800 (800 MHz) spectrometer. The sample was packed into a 2.5-mm zirconia rotor, and the measurement was carried out using two-pulse phase-modulated decoupling (30 kHz, 1 s recycle delay, 3 ms contact time, π/2 pulse width = 2.43 μs at 69.5 W, and 2048 scans). The CH₂ peak of the external adamantane standard was 29.5 ppm. Spectra were processed with Delta NMR Software (v 5.0) using conventional techniques (100 Hz line broadening window function). The position of Ni in Ni₂-CPD_{p_y}873(1) was analysed by the HAADF-STEM technique (Titan³ G2 60–300 Double Cs-Corrector, FEI Company; 300 V). Elemental analysis of the carbonized samples was carried out with a Yanaco JM10 analyser. The sample underwent combustion (flow = 20% O₂ + 80% He); gasses generated were converted into CO₂, H₂O, and N₂ to determine the respective C, H, and N amounts; Ni remained as oxidized ash. The Ni content was determined by assuming its composition as NiO; the amount of O was calculated by subtracting the amount of C, H, N, and Ni from the initial sample weight. Raman spectra were measured with a Jasco NRS-3100 (532.2 nm line). Absorption spectra were measured from samples moulded into KBr pellets (Nicolet 6700 FT-IR spectrometer, 0.04949–0.4959 eV/Perkin-Elmer Lambda750A UV-vis-NIR spectrometer, 0.4959–4.959 eV). The temperature-dependent electric resistance was measured with a two-electrode method for high resistance samples [Ni₂-CPD_{p_y}, Ni₂-CPD_{p_y}593(0), Ni₂-CPD_{p_y}873(1); pellet diameter = 3 mm] and a four-probe method for low resistance Ni₂-CPD_{p_y}973(1) (rod-shape: 3.0 × 0.68 × 0.37 mm). Ni₂-CPD_{p_y}873(1) and Ni₂-CPD_{p_y}973(1) were mixed with 5 wt% binder polymer (PTFE). The sample was placed in a Sumitomo SRDK-101D cryogenic refrigerating system. Electric contacts were prepared using Tokuriki #8560 gold paste and 25 μm gold wires. In the two-probe method, force-voltage current measurements were performed using a Keithley 6517 A electrometer. In the four-probe method, a constant current (0–2 μA) was applied (Advantest R6161). The voltage was measured by a Hewlett-Packard 3458 A digital multimeter. XPS spectra were measured with a JEOL JPS-9200. To avoid charge build-up, a solution of Ni₂-CPD_{p_y} in chloroform was spin-coated on an Al substrate (purity = 99.999, Al-Kα radiation, spot size = 3 mm). The substrate was heat treated (≤593 K) to prepare Ni₂-CPD_{p_y}593(0) and its XPS spectra were recorded. Subsequently, the substrate was heat treated (873 K, 1 h) to prepare Ni₂-CPD_{p_y}873(1) and its XPS spectra were recorded. Ni-K edge XAFS measurements, before and after carbonization of Ni₂-CPD_{p_y}, were performed in transmission mode (in air, room temperature, synchrotron radiation BL14B2 beam line, SPring-8). The recorded spectra were normalized and fitted by REX2000 (Rigaku). The precise Ni to N distance and coordination number were calculated from the EXAFS results by using FEFF8.2. Magnetic susceptibility data were collected in the temperature range of 5.0–300 K in an applied field of 10 kG using a Quantum Design MPMS2 SQUID magnetometer. X-band EPR data were recorded on a JEOL JES-FA100 spectrometer equipped with an Oxford ESR900 continuous-flow liquid He cryostat. N₂ and CO₂ adsorption isotherms were measured at 77 K and 298 K, respectively (MicrotracBEL Corp. BELMAX). In the N₂ adsorption isotherm, the specific surface area was calculated by the Brunauer-Emmett-Teller (BET) method in the pressure range of P/P₀ = 0.05–0.35, and the total pore volume (V_{N₂}) was calculated at P/P₀ = 0.96. In the CO₂ adsorption isotherm, the pore volume (V_{CO₂}) was calculated by the Dubinin-Radushkevich equation.

Data availability. Crystallographic data (CIF files) for Ni₂-CPD_{p_y} and Ni₂-CPD_{p_y}593(0) have been deposited with the Cambridge Crystallographic Data Centre as supplementary publications. CCDC 1552441 (Ni₂-CPD_{p_y}) and CCDC 1552442 (Ni₂-CPD_{p_y}593(0)) contain the supplementary crystallographic data. These data can be obtained free of charge from the Cambridge Crystallographic Data Centre via www.ccdc.cam.ac.uk/data_request/cif. PXRD analysis, construction of a model structure of Ni₂-CPD_{p_y}873(1), computational simulations, and CO₂ reduction measurements are provided in Supplementary Methods. All other data supporting the findings of this study are available within the article and its Supplementary Information.

Received: 12 January 2017 Accepted: 6 June 2017

Published online: 24 July 2017

References

- Fitzer, E., Mueller, K. & Schaefer, W. *The Chemistry of the Pyrolytic Conversion of Organic Compounds to Carbon* (Marcel Dekker, Inc., 1971).
- Nishihara, H. & Kyotani, T. Templated nanocarbons for energy storage. *Adv. Mater.* **24**, 4473–4498 (2012).
- Jaouen, F. et al. Recent advances in non-precious metal catalysis for oxygen-reduction reaction in polymer electrolyte fuel cells. *Energy Environ. Sci.* **4**, 114–130 (2011).
- Ikeda, T. et al. Carbon alloy catalysts: active sites for oxygen reduction reaction. *J. Phys. Chem. C* **112**, 14706–14709 (2008).
- Lefevre, M., Proietti, E., Jaouen, F. & Dodelet, J. P. Iron-based catalysts with improved oxygen reduction activity in polymer electrolyte fuel cells. *Science* **324**, 71–74 (2009).
- Wu, G., More, K. L., Johnston, C. M. & Zelenay, P. High-performance electrocatalysts for oxygen reduction derived from polyaniline, iron, and cobalt. *Science* **332**, 443–447 (2011).
- Jiang, H. L. et al. From metal-organic framework to nanoporous carbon: toward a very high surface area and hydrogen uptake. *J. Am. Chem. Soc.* **133**, 11854–11857 (2011).
- Yang, S. J. et al. Preparation and exceptional lithium anodic performance of porous carbon-coated ZnO quantum dots derived from a metal-organic framework. *J. Am. Chem. Soc.* **135**, 7394–7397 (2013).
- Lin, Q. P. et al. New heterometallic zirconium metalloporphyrin frameworks and their heteroatom-activated high-surface-area carbon derivatives. *J. Am. Chem. Soc.* **137**, 2235–2238 (2015).
- Radhakrishnan, L. et al. Preparation of microporous carbon fibers through carbonization of Al-based porous coordination polymer (Al-PCP) with furfuryl alcohol. *Chem. Mater.* **23**, 1225–1231 (2011).
- Hu, M. et al. Direct synthesis of nanoporous carbon nitride fibers using Al-based porous coordination polymers (Al-PCPs). *Chem. Commun.* **47**, 8124–8126 (2011).
- Chaikititilip, W. et al. Nanoporous carbons through direct carbonization of a zeolitic imidazolate framework for supercapacitor electrodes. *Chem. Commun.* **48**, 7259–7261 (2012).
- Hu, M. et al. Direct carbonization of Al-based porous coordination polymer for synthesis of nanoporous carbon. *J. Am. Chem. Soc.* **134**, 2864–2867 (2012).
- Yang, S. J. et al. MOF-derived hierarchically porous carbon with exceptional porosity and hydrogen storage capacity. *Chem. Mater.* **24**, 464–470 (2012).
- Kayahara, E. et al. Synthesis and physical properties of a ball-like three-dimensional π-conjugated molecule. *Nat. Commun.* **4**, 2694 (2013).
- Torad, N. L. et al. Facile synthesis of nanoporous carbons with controlled particle sizes by direct carbonization of monodispersed ZIF-8 crystals. *Chem. Commun.* **49**, 2521–2523 (2013).
- Shrestha, L. K. et al. Nanoporous carbon tubes from fullerene crystals as the π-electron carbon source. *Angew. Chem. Int. Ed.* **54**, 951–955 (2015).
- Ogoshi, T. et al. Porous carbon fibers containing pores with sizes controlled at the angstrom level by the cavity size of pillar[6]arene. *Angew. Chem. Int. Ed.* **54**, 6466–6469 (2015).
- Tanaka, S., Nishiyama, N., Egashira, Y. & Ueyama, K. Synthesis of ordered mesoporous carbons with channel structure from an organic-organic nanocomposite. *Chem. Commun.* **28**, 2125–2127 (2005).
- Meng, Y. et al. Ordered mesoporous polymers and homologous carbon frameworks: amphiphilic surfactant templating and direct transformation. *Angew. Chem. Int. Ed.* **44**, 7053–7059 (2005).
- Liang, C. D. et al. Synthesis of a large-scale highly ordered porous carbon film by self-assembly of block copolymers. *Angew. Chem. Int. Ed.* **43**, 5785–5789 (2004).
- Nobukuni, H., Shimazaki, Y., Tani, F. & Naruta, Y. A nanotube of cyclic porphyrin dimers connected by nonclassical hydrogen bonds and its inclusion of C₆₀ in a linear arrangement. *Angew. Chem. Int. Ed.* **46**, 8975–8978 (2007).
- Maruyama, J. et al. Carbonaceous hydrogen-evolution catalyst containing cobalt surrounded by a tuned local structure. *Chem. Cat. Chem.* **6**, 2197–2200 (2014).
- Maruyama, J., Shinagawa, T., Siroma, Z. & Mineshige, A. One-pot hybrid physical-chemical vapor deposition for formation of carbonaceous thin film with catalytic activity for oxygen reduction. *Electrochem. Commun.* **13**, 1451–1454 (2011).
- Nobukuni, H. et al. Supramolecular structures and photoelectronic properties of the inclusion complex of a cyclic free-base porphyrin dimer and C₆₀. *Chem. Eur. J* **16**, 11611–11623 (2010).
- Corriu, R. J. P. et al. Organosilicon polymers—pyrolysis chemistry of poly [(dimethylsilylene)diacetylene]. *Organometallics* **11**, 2507–2513 (1992).

27. Echkhardt, H., Prusik, T. & Chance, R. R. *Solid-State Photopolymerization of Diacetylenes* (Springer-Science+Business Media, B.V., 1985).
28. Altomare, A. et al. New techniques for indexing: N-TREOR in EXPO. *J. Appl. Cryst.* **33**, 1180–1186 (2000).
29. Favre-Nicolin, V. & Cerny, R. FOX, 'free objects for crystallography': a modular approach to *ab initio* structure determination from powder diffraction. *J. Appl. Cryst.* **35**, 734–743 (2002).
30. Visser, J. W. A fully automatic program for finding the unit cell from powder data. *J. Appl. Cryst.* **2**, 89–95 (1969).
31. Rietveld, H. M. A profile refinement method for nuclear and magnetic structures. *J. Appl. Cryst.* **2**, 65–71 (1969).
32. Xu, R., Gramlich, V. & Frauenrath, H. Alternating diacetylene copolymer utilizing perfluorophenyl-phenyl interactions. *J. Am. Chem. Soc.* **128**, 5541–5547 (2006).
33. Lu, G. L. et al. Metallated porphyrin based porous organic polymers as efficient electrocatalysts. *Nanoscale* **7**, 18271–18277 (2015).
34. Ziegelbauer, J. M. et al. Direct spectroscopic observation of the structural origin of peroxide generation from Co-based pyrolyzed porphyrins for ORR applications. *J. Phys. Chem. C* **112**, 8839–8849 (2008).
35. Frisch, M. J. et al. Connecticut: Gaussian 09, Revision D.01 (Gaussian, Inc. 2009).
36. Kawashima, Y. & Katagiri, G. Fundamentals, overtones, and combinations in the raman spectrum of graphite. *Phys. Rev. B* **52**, 10053–10059 (1995).
37. Brown, S. D. M. et al. Origin of the Breit-Wigner-Fano lineshape of the tangential G-band feature of metallic carbon nanotubes. *Phys. Rev. B* **63**, 155414 (2001).
38. Jorio, A., Saito, R., Dresselhaus, G. & Dresselhaus, M. S. Determination of nanotubes properties by raman spectroscopy. *Philos. Trans. R. Soc. A Math. Phys. Eng. Sci.* **362**, 2311–2336 (2004).
39. Dresselhaus, M. S., Dresselhaus, G., Saito, R. & Jorio, A. Raman spectroscopy of carbon nanotubes. *Phys. Rep.* **409**, 47–99 (2005).
40. Yamada, Y. et al. Analysis of heat-treated graphite oxide by X-ray photoelectron spectroscopy. *J. Membr. Sci.* **48**, 8171–8198 (2013).
41. Furlan, A. et al. Crystallization characteristics and chemical bonding properties of nickel carbide thin film nanocomposites. *J. Phys. Condens. Matter.* **26**, 415501 (2014).
42. Kim, J. et al. Pyrolysis of epoxidized fullerenes analyzed by spectroscopies. *J. Phys. Chem. C* **118**, 7076–7084 (2014).
43. Yamada, Y., Kim, J., Matsuo, S. & Sato, S. Nitrogen-containing graphene analyzed by X-ray photoelectron spectroscopy. *Carbon. NY* **70**, 59–74 (2014).
44. Kim, J. et al. Spectral change of simulated X-ray photoelectron spectroscopy from graphene to fullerene. *J. Membr. Sci.* **50**, 6739–6747 (2015).
45. Czekaj, I. et al. Characterization of surface processes at the Ni-based catalyst during the methanation of biomass-derived synthesis gas: X-ray photoelectron spectroscopy (XPS). *Appl. Catal. A* **329**, 68–78 (2007).
46. Kwag, G., Park, E. & Kim, S. Self-assembled and alternative porphyrin-phthalocyanine array. *Bull. Korean Chem. Soc.* **25**, 298–300 (2004).
47. Miller, J. T., Fisher, R. B., van der Eerden, A. M. J. & Koningsberger, D. C. Structural determination by XAFS spectroscopy of non-porphyrin nickel and vanadium in Maya residuum, hydrocracked residuum, and toluene-insoluble solid. *Energy Fuels* **13**, 719–727 (1999).
48. DeBlase, C. R. et al. Rapid and efficient redox processes within 2D covalent organic framework thin films. *ACS Nano* **9**, 3178–3183 (2015).
49. Iwase, K. et al. Copper-modified covalent triazine frameworks as non-noble-metal electrocatalysts for oxygen reduction. *Angew. Chem. Int. Ed.* **54**, 11068–11072 (2015).
50. Li, B. et al. Metal organic frameworks as highly active electrocatalysts for high-energy density, aqueous zinc-polyiodide redox flow batteries. *Nano Lett.* **16**, 4335–4340 (2016).
51. Kelly, C. A. et al. The thermodynamics and kinetics of CO₂ and H⁺ binding to Ni(cyclam)⁺ in aqueous solution. *J. Am. Chem. Soc.* **117**, 4911–4919 (1995).
52. Froehlich, J. D. & Kubiak, C. P. Homogeneous CO₂ reduction by Ni(cyclam) at a glassy carbon electrode. *Inorg. Chem.* **51**, 3932–3934 (2012).
53. Song, J., Klein, E. L., Neese, F. & Ye, S. The mechanism of homogeneous CO₂ reduction by Ni(cyclam): Product selectivity, concerted proton–electron transfer and C–O bond cleavage. *Inorg. Chem.* **53**, 7500–7507 (2014).
54. Froehlich, J. D. & Kubiak, C. P. The homogeneous reduction of CO₂ by [Ni(cyclam)]⁺: Increased catalytic rates with the addition of a CO scavenger. *J. Am. Chem. Soc.* **137**, 3565–3573 (2015).
55. Su, P. et al. Nickel-nitrogen-modified graphene: An efficient electrocatalyst for the reduction of carbon dioxide to carbon monoxide. *Small.* **12**, 6083–6089 (2016).
56. Nishihara, H. et al. A possible buckyowl-like structure of zeolite templated carbon. *Carbon. NY* **47**, 1220–1230 (2009).
57. Kasai, H. et al. A novel preparation method of organic microcrystals. *Jpn J. Appl. Phys. Part 2* **31**, L1132–L1134 (1992).
58. Komai, Y. et al. Size and form control of titanilphthalocyanine microcrystals by supercritical fluid crystallization method. *Mol. Cryst. Liq. Cryst.* **322**, 167–172 (1998).
59. Takahashi, Y., Kasai, H., Nakanishi, H. & Suzuki, T. M. Test strips for heavy-metal ions fabricated from nanosized dye compounds. *Angew. Chem. Int. Ed.* **45**, 913–916 (2006).
60. Kikuchi, T. et al. Novel development for fabrication of size- and morphology-controlled titanilphthalocyanine nanocrystals. *Chem. Lett.* **44**, 1232–1233 (2015).
61. Itoi, H., Nishihara, H., Kogure, T. & Kyotani, T. Three-dimensionally arrayed and mutually connected 1.2-nm nanopores for high-performance electric double layer capacitor. *J. Am. Chem. Soc.* **133**, 1165–1167 (2011).

Acknowledgements

This work was supported by PRESTO, JST; JSPS KAKENHI Grant Number 15KK0196; the Dynamic Alliance for Open Innovation Bridging Human, Environment and Materials; and the Network Joint Research Centre for Materials and Devices. The PXRD and XAFS measurements were performed in SPring-8 (Proposals no. 2015A1956, 2015A1666, and 2016A1750). We thank Tohoku University Molecule and Material Synthesis Platform in Nanotechnology Platform Project, for ¹³C CP-MAS NMR analysis operated by Mr. Shinichiro Yoshida. The authors acknowledge Prof. T. Kyotani for his advice, Dr A. Castro Muniz for his experimental support, Prof. M. Kakihana for performing Raman spectroscopy, Rigaku Co. for their kind support for TPD measurements with TG-PI-MS. The authors express the deepest gratitude to Professor K. Kaneko for his valuable advice.

Author contributions

H.T.N. designed the project, summarized all the data provided by co-authors, and wrote the manuscript. F.T. synthesized Ni₂-CPD_{py} and H₄-CPD_{py} and supervised the outline of this work from the viewpoint of organic chemistry. H.F.N. developed the synthetic methods of Ni₂-CPD_{py} and H₄-CPD_{py}, and further improved the methods to provide sufficient amount of these substances. T.T.H. carried out TG of organic crystals, and found the retention of the ordered structure by TEM. Then, he characterized the materials with Raman spectroscopy and XPS. K.M. carried out elemental analysis of the materials. T.K. taught H.T.N. and T.T.H. the synthesis of Ni₂-CPD_{py} and H₄-CPD_{py}, and also contributed to the preparation of their solvent-free crystals. M. O. carried out DSC measurements and gas adsorption measurements. T.K.H. analysed OCFs by high-resolution TEM together with fast Fourier transform, and H.J. supervised the experiment and data analysis. T.A. suggested and designed the analysis of materials by electrical conductivity, EPR, Magnetic susceptibility, and UV-vis absorption spectroscopy, and N.H. carried out these measurements and data analyses. H.T.K. suggested the control of crystal morphology by using the reprecipitation method, and Y.K. carried out the experiment. J.M. carried out XAFS and electrochemical measurements, as well as the data analyses. Y.M. contributed the structural analysis of the carbonized samples. Y.H. performed STEM-HAADF observations of OCFs and analysed the data. H.S.K. revealed the crystal structures of Ni₂-CPD_{py} and Ni₂-CPD_{py}593(0) from their PXRD patterns. Y.Y. carried out the simulation of Raman spectra and XRS spectra of the samples and analysed the experimental data according to the calculation results. K.K. designed the electrochemical CO₂ reduction reaction, and S.Y. performed the measurements and analyses.

Additional information

Supplementary Information accompanies this paper at doi:10.1038/s41467-017-00152-z.

Competing interests: The authors declare no competing financial interests.

Reprints and permission information is available online at <http://npg.nature.com/reprintsandpermissions/>

Publisher's note: Springer Nature remains neutral with regard to jurisdictional claims in published maps and institutional affiliations.



Open Access This article is licensed under a Creative Commons Attribution 4.0 International License, which permits use, sharing, adaptation, distribution and reproduction in any medium or format, as long as you give appropriate credit to the original author(s) and the source, provide a link to the Creative Commons license, and indicate if changes were made. The images or other third party material in this article are included in the article's Creative Commons license, unless indicated otherwise in a credit line to the material. If material is not included in the article's Creative Commons license and your intended use is not permitted by statutory regulation or exceeds the permitted use, you will need to obtain permission directly from the copyright holder. To view a copy of this license, visit <http://creativecommons.org/licenses/by/4.0/>.

© The Author(s) 2017